nature communications

Article

https://doi.org/10.1038/s41467-026-70549-2

Embryonic zeolite-mediated suture synthesis of thin and scalable zeolite membranes for tailored gas separation

Received: 19 October 2025

Accepted: 24 February 2026

Published online: 13 March 2026

Check for updates

Lekai You[1], Yang Jin[1], Zerui Zhu[1], Xingyu Peng[1], Yuanxing Fan[2], Freek Kapteijn[3], Xuerui Wang[1,2] ✉ & Xuehong Gu[1,2] ✉

Zeolite membranes exhibit considerable potential for gas separation; however, two critical challenges (low permeation flux and scaling-up fabrication) continue to hinder their practical implementation. Here, we propose an embryonic zeolite-mediated suture (EZMS) strategy to synthesize large-area zeolite membranes with stable gas separation performance. The membrane thickness is equivalent to that of the initial seed layer—a feature validated across three distinct zeolite frameworks (STT, CHA, and MFI). For high-silica CHA (also known as SSZ-13) zeolite membranes, the EZMS strategy enables a 5-fold thickness reduction, yielding a CO_2 permeance of 1.02×10^{-6} mol·m^{-2}·s^{-1}·Pa^{-1} (3000 GPU) and a CO_2/CH_4 selectivity of 158 at 0.2 MPa. Scalability is validated by the successful synthesis of SSZ-13 zeolite membrane bundles with an individual area of 0.5 m^2 (40 cm in length). The membranes exhibited excellent high-pressure resistance (>4 MPa) and long-term stability (>220 d) for humid CO_2/CH_4 separation, representing a high-performance benchmark for biogas upgrading. The reliable synthesis protocol and improved performance highlight the industrial application potential of zeolite membranes.

Membrane gas separation is a compelling energy-efficient alternative to amine absorption and cryogenic distillation for natural gas upgrading. Polymeric membranes dominate current commercial applications; however, their susceptibility to plasticization under high partial pressures of CO_2 and H_2S severely limits their lifetime and separation efficiency[1,2]. In contrast, polycrystalline membranes—such as metal-organic frameworks (MOFs)[3,4], covalent organic frameworks (COFs)[5] and zeolites[6]—are promising candidates to overcome these limitations, owing to their inherent chemical and mechanical robustness. Moreover, polycrystalline membranes show great potential for helium purification and hydrocarbon isomer separation[7]. Nevertheless, their practical application is hindered by low permeation flux and scalable manufacturing challenges[1].

The permeation flux is inversely proportional to thickness according to the generalized Maxwell-Stefan model[8]. To prepare ultrathin polycrystalline membranes, novel interfacial synthesis methods and two-dimensional (2D) nanosheet building blocks have been explored[9–11]. For instance, the Zr-*fum*$_{67}$-*mes*$_{33}$-fcu-MOF membrane thickness was reduced to 30 nm via electrochemical synthesis, leading to an improved N_2 permeance of 3057 GPU (Gas Permeation Unit, 1 GPU = 3.3928×10^{-10} mol·m^{-2}·s^{-1}·Pa^{-1})[9]. Similarly, the thickness of 2D CuBDC membranes was reduced to <10 nm by precisely regulating the stacking of MOF nanosheets[10,11]. However, the fabrication of these ultrathin polycrystalline membranes is extremely complicated, as conductive Pt coating or nanosheet exfoliation is essential[9]. Furthermore, suitable 2D zeolite nanosheets for gas separation membranes are significantly scarce. Only ten-membered ring (10MR) MFI[12] and six-membered ring (6MR) RUB-15[13] zeolite nanosheets have been utilized as building blocks; meanwhile, they are retransformed into a three-dimensional structure following secondary growth or high-

[1]State Key Laboratory of Materials-Oriented Chemical Engineering, College of Chemical Engineering, Nanjing Tech University, Nanjing, PR China. [2]Quzhou Membrane Material Innovation Institute, Quzhou, PR China. [3]Chemical Engineering Department, Delft University of Technology, Van der Maasweg 9, Delft, The Netherlands. ✉e-mail: x.wang@njtech.edu.cn; xhgu@njtech.edu.cn

temperature calcination. Alternatively, nano-seeds are more suitable for synthesizing thin zeolite membranes via dry gel conversion[14], gelless[15] or hot-dipping methods[16]. The final membrane thickness is generally tenfold higher than that of the seed layer due to outward intergrowth from the substrates following the classical crystallization pathways[17]. Therefore, preparing large-area gas separation zeolite membranes with a thickness of <1 μm remains extremely challenging[2,18].

Various zeolite membrane geometries have also been reported to enhance permeation flux, such as hollow fibers (HFs)[19], single tubes[20], and multi-channel monoliths[21–23]. However, all these membranes have a limited effective area for each batch synthesis. Lee et al. fabricated six 12-cm-long SAPO-34 zeolite membranes in one autoclave, with a reproducibility error of 10%[24]. Recently, we successfully synthesized nine 40-cm-long hollow fiber SSZ-13 zeolite membranes in one autoclave using interzeolite-converted seeds. However, CO_2 permeance was only 1200 GPU due to the relatively thick zeolite membrane (2.8 μm)[18]. Nair et al. prepared twenty 6.5-cm-long hollow fiber SSZ-13 zeolite membranes in one batch, but no reproducibility in gas separation performance was reported[19]. These limitations originate from the classical layer-by-layer mechanism intrinsic to the conventional secondary growth method[25], wherein deposited seeds grow via the conversion of amorphous precursors—an inherently restrictive process creating an unavoidable trade-off between thickness control and defect elimination[26]. Therefore, the lack of a reliable synthesis protocol for large-area gas separation zeolite membranes has become a critical barrier to their successful practical implementation.

Herein, we present an embryonic zeolite-mediated suture strategy (Fig. 1), enabling the scalable fabrication of thin and highly selective zeolite membranes for tailored gas separation. The amorphous precursors are first converted into short-range ordered embryonic zeolites, and these highly reactive intermediates facilitate the seamless suturing of ball-milled seed particles via rapid condensation reactions. This method deliberately avoids classical crystallization pathways, which typically result in unregulated membrane thickening and defect formation in zeolite membranes. This alternative strategy not only maintains the geometric integrity of the seed layer to ensure precise thickness control but also minimizes defect generation, thereby simultaneously enhancing permeation flux and selectivity. We demonstrate the universality of the EZMS strategy across three distinct zeolite topological frameworks (7MR and 9MR STT, 8MR CHA, and 10MR MFI) for He/CH_4, CO_2/CH_4, and *n*-/*i*-butane mixture separation, respectively. The scalability is further validated through the batch synthesis of large-area SSZ-13 zeolite membrane bundles. We also evaluated the separation performance and long-term stability for the integrated removal of CO_2, H_2S, and moisture in biogas upgrading.

Results and discussion

Zeolite membrane synthesis and characterization

Three distinct zeolite membranes (STT, CHA, and MFI) were synthesized using the EZMS strategy. Ball-milled seeds were uniformly coated onto four-channel hollow fibers through a single-step dip-coating method (Fig. S1). After secondary growth, all membranes exhibited a well-intergrown surface (Fig. 2a, c, e), a typical morphology of high-selective zeolite membranes[18]. Unlike conventional zeolite membranes that typically exhibit a ~10-fold thickness amplification during hydrothermal synthesis[2,17], the final thickness of our membranes remained nearly identical to their initial seed layers (Fig. 2b, d, f). To further confirm EZMS strategy's thickness control capability, a total of five SSZ-13 zeolite membranes were synthesized using seed layers with thicknesses ranging from 540 ± 30 nm to 1600 ± 100 nm (Table S1 and Fig. S2). All these membranes exhibited a final thickness consistent with their initial seed layers. This result confirms EZMS strategy is effective in controlling membrane thickness over a broad range.

To investigate the kinetics of EZMS-derived zeolite membranes formation, the evolution of a 950 nm-thick SSZ-13 zeolite seed layer was monitored via time-resolved SEM and elemental analysis of Si/Al ratio (SAR). During the early synthesis stage (0.5–2.5 h), the substrate was covered with irregular aggregates (thickness: 1.0 ± 0.2 μm, Fig. S3a–f). The SAR was lower than both the initial seed SAR (50, Fig. S4) and the precursor SAR (105, Fig. S5), which is attributed to gaps between discrete seed particles. These gaps exposed the Al-rich substrate, leading to the inclusion of extra Al signals in the analysis and thereby reducing the measured SAR. When the synthesis duration exceeded 4 h, irregular aggregates gradually transformed into well-defined cubic crystals (Fig. S3g, h). This crystallization filled the interparticle gaps, eliminating the substrate-derived Al signal. Consequently, the membrane SAR finally stabilized at ~40, consistent with the typical high-silica CHA zeolites[27]. Intriguingly, in the subsequent crystallization stage (4–24 h), both surface crystal size and membrane

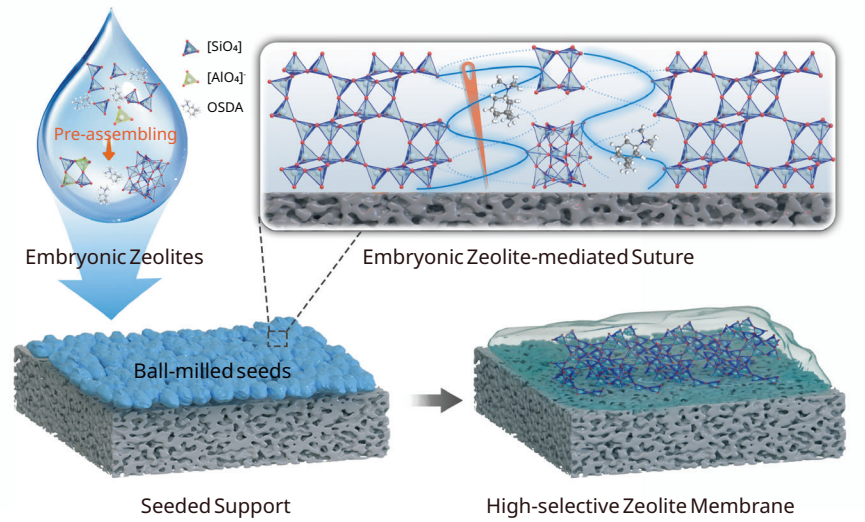

Fig. 1 | Illustration of embryonic zeolite-mediated suture strategy. In pre-assembly period, silicon (Si), aluminum (Al) precursors and organic structure directing agent (OSDA) were initially assembled into embryonic zeolites, then participated in the condensation reactions with the pre-deposited ball-milled seed particles, ultimately stitching the discrete into continuous and highly selective zeolite membranes.

https://doi.org/10.1038/s41467-026-70549-2

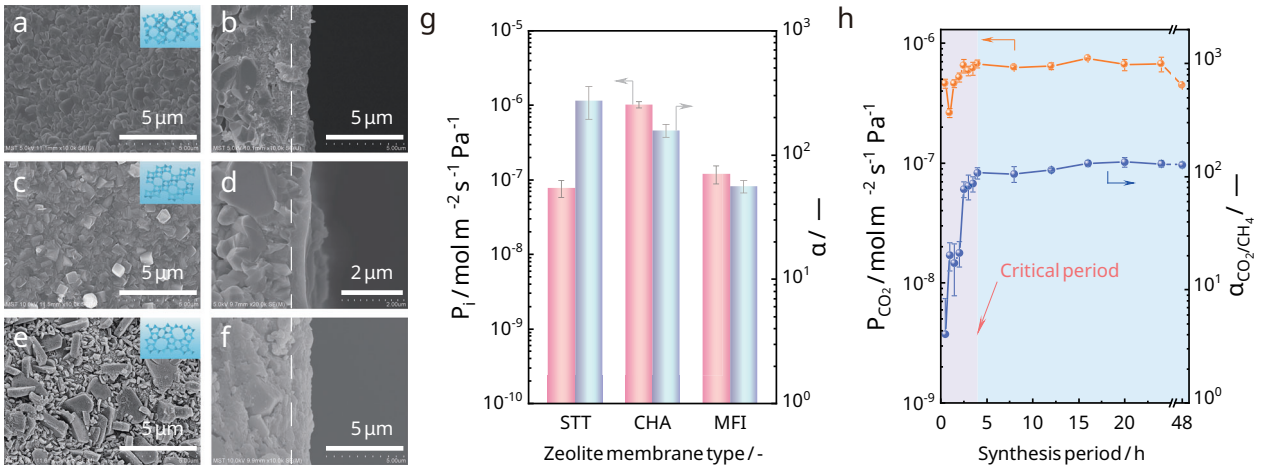

Fig. 2 | Characterization of three distinct zeolite membranes synthesized via EZMS strategy. SEM images of STT (**a**, **b**), SSZ-13 (**c**, **d**), and MFI (**e**, **f**) zeolite membranes; insert: topological framework of the corresponding zeolite. **g** Gas separation performance towards tailored gas pairs of He/CH_4 for STT, CO_2/CH_4 for SSZ-13, and *n*-/*i*-C_4H_{10} for MFI zeolite membranes. Synthesis conditions: STT and SSZ-13 zeolite membranes were synthesized at 180 °C for 24 h; MFI zeolite membranes were synthesized at 160 °C for 14 h. Gas separation test conditions: Feed gas was a 200 mL·min^{-1} equimolar binary mixture at 298 K and 0.2 MPa for all membranes; a 50 mL·min^{-1} He sweep gas was applied at atmospheric pressure for STT and SSZ-13 zeolite membranes, and no sweep gas was used for MFI zeolite membranes. **h** Effect of synthesis period on CO_2/CH_4 separation performance of SSZ-13 zeolite membranes synthesized at 180 °C. Error bars represent the standard deviation from three independent measurements.

thickness remained constant (Figs. S3i–l and Fig. S6). This observation further proves the EZMS strategy suppresses uncontrolled overgrowth and achieves precise thickness control.

Membrane quality was further evaluated through binary gas mixture tests tailored to the topological feature of each zeolite membrane. The STT, SSZ-13, and MFI zeolite membranes exhibited selectivities of 275 for He/CH_4, 158 for CO_2/CH_4, and 56 for *n*-/*i*-C_4H_{10} binary mixture separation, respectively (Fig. 2g). These values are significantly higher than the corresponding Knudsen selectivities, confirming that the interzeolite gaps have been effectively eliminated and the gas separation is primarily governed by the intrinsic zeolitic channels. Subsequently, an equimolar CO_2/CH_4 mixture was used to probe the SSZ-13 zeolite membrane evolution with synthesis time (Fig. 2h) and thickness. Initially, the CO_2/CH_4 selectivity was relatively low, which is another evidence of gaps between seed particles and precursor species. The selectivity exceeded 100 and plateaued once the synthesis time extended to 4 h. This result proves a critical period of 4 h for SSZ-13 zeolite membrane synthesis, which is reduced by 83% compared to the conventional synthesis protocol[18]. CO_2 permeance increased significantly with decreasing membrane thickness (Table S2). The 560-nm-thick membrane achieved a CO_2 permeance of 1.02×10^{-6} mol·m^{-2}·s^{-1}·Pa^{-1} (3000 GPU) and a CO_2/CH_4 selectivity of 158. The performance not only far exceeds Robeson's upper bound but also ranks among the state-of-the-art for CO_2/CH_4 separation membranes (Figs. S7 and S8)[28,29].

Zeolite membrane formation mechanism

To elucidate the thickness control mechanism of the EZMS strategy, the precursor's pre-assembly period (t_1 = 0, 12, 84 h) was significantly investigated. A Q^4Si(1Al) signal at −104.7 ppm was instantaneously observed in ^{29}Si MAS NMR spectra (Fig. 3a), indicating a rapid condensation reaction between silicon sources and aluminum species, which is the initial step of embryonic zeolite formation[30]. With an extended pre-assembly period to 84 h, the peak area of Q^4Si(2Al) signal at −99.2 ppm increased monotonously and reached 25.4% (Fig. S9). This result confirms that more aluminum atoms are incorporated into 4MRs following Lowenstein's rule[31]. The formation of quaternary ring structures was further verified through electrospray-ionization mass spectrometry (ESI-MS, Fig. S10)[32,33]. In the ^{27}Al MAS NMR spectra (Fig. 3b), the Al signal shifted from 61.1 ppm to 53.3 ppm. The result confirms an increased Al-O-Si bond angle in the precursor, which is favorable for the formation of embryonic zeolite[30]. Only the tetrahedral-coordinated Al signal (no octahedral Al at ~0 ppm) is detected, confirming that Al species are uniformly integrated into the zeolite framework. Additionally, the narrowed full width at half-maximum (FWHM) of both the Q^4Si(2Al) and tetrahedral Al peaks indicated the formation of more ordered precursor species[34].

To further characterize the ordered structure in the precursor, ATR-FTIR (Fig. 3c) and FTIR (Fig. S11) analysis were performed. The peak at 1060 cm^{-1} is assigned to the asymmetric vibration of T-O bonds, which is well explained by the incorporation of Al atoms into the frameworks[35,36]. The peaks at 652 and 629 cm^{-1} are assigned to the 4MR-related structures, which are consistent with the ^{29}Si MAS NMR and ESI-MS results. With an 84 h pre-assembly period, the increase in peak intensity at 543 cm^{-1} revealed the assembly of 4MRs into double six-membered rings (*d6r*), which is a key intermediate structure for CHA zeolite framework formation[35]. Since the UV Raman signals at 472 and 319 cm^{-1} overlapped with those derived from $TMAda^+$ cations (Fig. S12)[36], the increased intensity was assigned to newly formed 4MRs and 6MRs. Additionally, the enhanced signal at 197 cm^{-1} further revealed the formation of *cha* cages[37]. In the high-resolution transmission electron microscopy (HR-TEM) and selected area electron diffraction (SAED, Fig. 3d and Figs. S13 and S14), an electron diffraction ring associated with (3 3 3) crystal plane of CHA zeolite was observed. However, the precursor remained amorphous in powder X-ray diffraction (PXRD) analysis (Fig. S15). The result confirms the absence of long-range crystalline order, which is a defining structural characteristic of embryonic zeolites as reported[38].

To probe the role of $TMAda^+$ in *cha* cage formation, the precursor was analyzed by thermogravimetric analysis (TGA) and solid-state ^{13}C CP MAS NMR spectroscopy. The weight loss of crystalline SSZ-13 zeolite is primarily triggered at temperatures above 350 °C (Fig. S16). While the precursor exhibited predominant weight loss between 100 and 250 °C, which is due to evaporation and decomposition of water and $TMAda^+$. Intriguingly, a secondary weight loss was observed between 300 and 550 °C, which is due to the removal of $TMAda^+$

https://doi.org/10.1038/s41467-026-70549-2

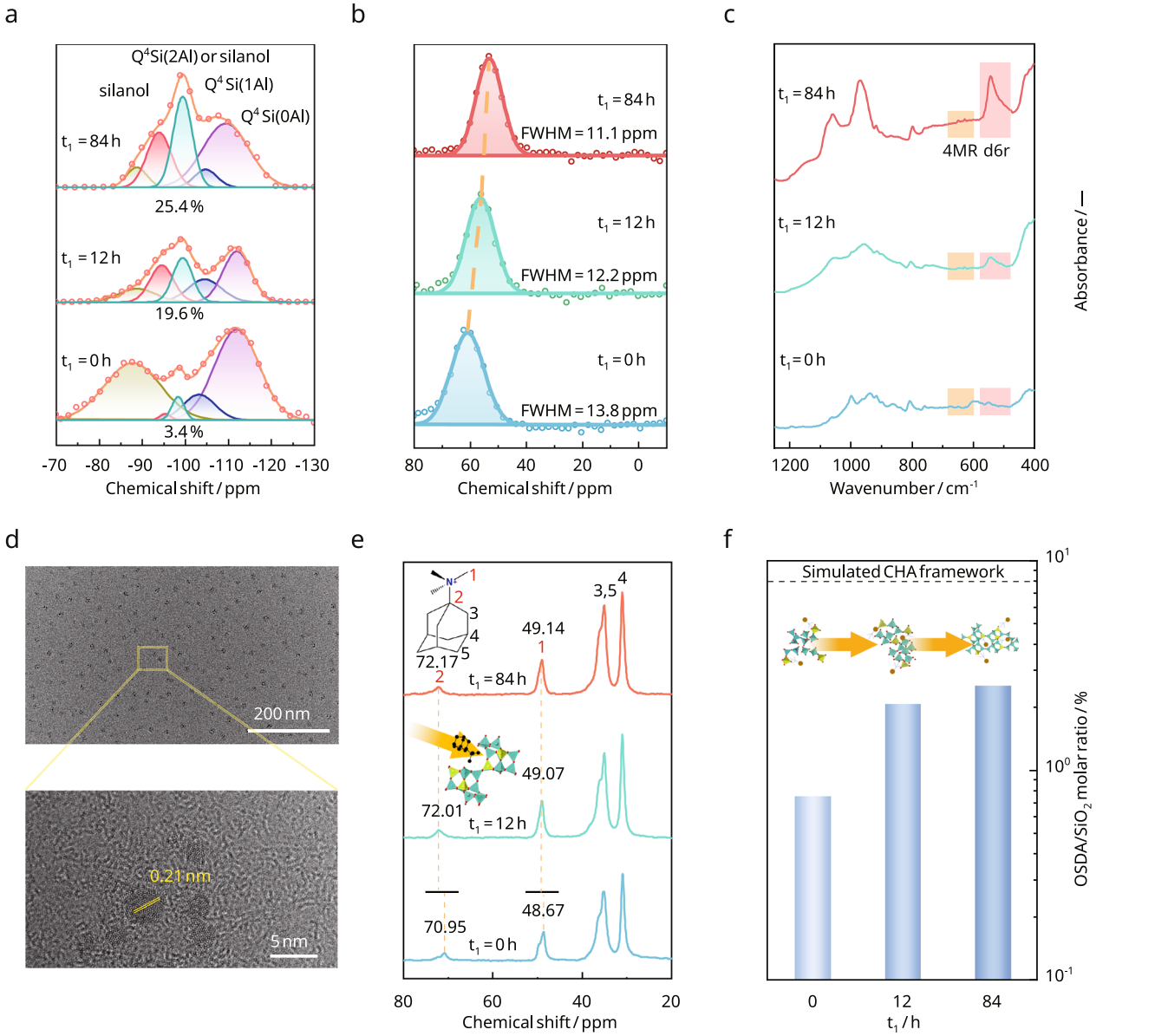

Fig. 3 | Effect of pre-assembly period (t_1) on precursor evolution. a, **b** ^{29}Si and ^{27}Al MAS NMR spectra of the gel. **c** ATR-FTIR spectra of the gel, the yellow region corresponds to the 4MR vibration, while the red region indicates the *d6r* vibration. **d** TEM and HR-TEM of the gel with pre-assembly period of t_1 = 84 h, **e** ^{13}C CP MAS NMR spectra of the gel. Inset: molecular structure of TMAdaOH, with carbon atoms at distinct chemical environments labeled by numbers. **f** OSDA/SiO_2 of the gel calculated by TGA. Inset: schematic illustration of the local environment in the gel, where yellow spheres with tails represent TMAdaOH molecules, blue triangles represent Si atoms, yellow triangles denote Al atoms, and red spheres indicate O atoms.

trapped in the ordered structures (including *cha* cages)[39]. The solid-state ^{13}C CP MAS NMR spectra demonstrated a shift to a lower magnetic field, confirming the $TMAda^+$ cations were more tightly enclosed in the ordered structures (Fig. 3e)[36]. The amount of trapped $TMAda^+$ was quantified by calculating the molar ratio of trapped OSDA to SiO_2 (Fig. 3f), reaching 2.6% after an 84 h pre-assembly period. This value is 3.4 times higher than that in the initial precursor (without pre-assembly) but far lower than that in fully crystalline SSZ-13 zeolite (8.3%)[40]. This result indicates that the pre-assembly promotes $TMAda^+$ encapsulation in the ordered structures, though the precursor has not yet formed a well-crystallized zeolite.

The interaction between the seeds and the precursor was further investigated to elaborate on the zeolite membrane formation mechanism. Well-intergrown and highly selective membranes were successfully prepared via the aforementioned EZMS strategy, whereas only sparse crystals were observed when using the conventional dry gel method (Fig. S17). The short pre-assembly period of t_1 = 0 h and t_1 = 12 h caused worse intergrowth (Figs. S18 and S19) and significantly reduced CO_2/CH_4 selectivity (Fig. S20 and Table S3). Both results confirmed that sufficient pre-assembly is essential to generate ordered structures (e.g., 4MR, *d6r*, CHA-type cages), which are required for effective integration of the ball-milled seed particles. This explains why conventional hydrothermal synthesis typically requires a long duration of 96 h[41]. The CO_2/CH_4 selectivity of membranes prepared using hydrothermally synthesized seeds was merely 24 (Fig. S21), which is five times lower than that of membranes using ball-milled seeds. Furthermore, membranes synthesized via the in-situ method (Table S4) were even non-selective towards CO_2/CH_4 separation, which is attributed to poor intergrowth (Fig. S22). These membranes also exhibited slightly lower permeance, likely due to insufficient crystallization that left amorphous substance blocking the zeolitic channels[30]. Following this line, we propose an integration mechanism for EZMS-derived

https://doi.org/10.1038/s41467-026-70549-2

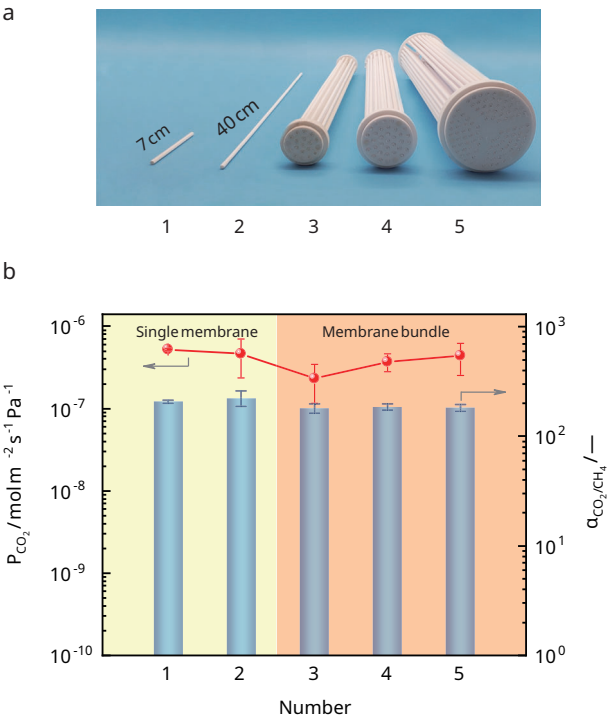

Fig. 4 | Large-area zeolite membranes and zeolite membrane bundles synthesized via the EZMS strategy. a Photo of single membrane (Number 1, 2) and the membrane bundles composed of 17 (Number 3), 33 (Number 4), and 102 (Number 5) single membranes. **b** Binary equimolar CO_2/CH_4 mixture separation performance at room temperature and 0.3 MPa (no sweep gas used). Error bars represent the standard deviation of four independent measurements.

membranes, wherein the ball-milled seed particles featuring abundant Si–OH groups[42] are firstly coated onto porous substrates, serving as anchoring sites for the ordered structures (e.g., *cha* cages, 4MR, 6MR, and *d6r*) in the pre-assembled precursor. The ordered precursor structures then bridge the fractured surfaces of adjacent seed particles via condensation reactions between their silanol groups and those on the seed surface, forming a continuous and defect-minimized zeolite membrane.

Large-area zeolite membrane synthesis optimization

To validate the feasibility of scaling up, we successfully synthesized 40-cm-long hollow fiber membranes (Fig. 4a). Our method led to a uniform layer thickness of 2.5 ± 0.6 μm along the axial direction (Fig. S23), which is also identical to that of the seed layer (Fig. S24). This contrasts sharply with the conventional method[41], which produced a significant thickness gradient from 3 μm at the top to 100 μm at the bottom (Fig. S25). The membrane quality was evaluated using an equimolar CO_2/CH_4 mixture at 0.3 MPa. The conventionally synthesized membranes exhibited a significant decline in selectivity from 149 ± 84 at the top to 18.5 ± 16.5 at the bottom along the axial direction (M11–M14, Table S5). However, the entire membrane synthesized using our EZMS strategy showed exceptional uniformity of CO_2/CH_4 selectivities exceeding 150 along the entire axial direction (M15–M18, Table S5). Subsequently, the scaled-up synthesis was extended from a single HF membrane to membrane bundles, each composed of 17, 33, and 102 HF membranes with effective areas of 0.08, 0.15, and 0.5 m^2, respectively. To the best of our knowledge, this latter is the largest SSZ-13 zeolite membrane for gas separation reported to date, which is approximately twentyfold larger than a single tube (0.019 m^2)[43] or multi-channel geometry membranes (0.024 m^2)[23]. The integration of the 0.5 m^2 membrane element into stainless-steel housing is demonstrated in Supplementary Video 1. All the membranes and membrane bundles exhibited a CO_2/CH_4 selectivity above 150 (Fig. 4b and Table S6). Furthermore, more than a dozen SSZ-13 zeolite membrane bundles, each with an effective area of 0.5 m^2, were fabricated to confirm superior reproducibility and scalability (Fig. S26).

Biogas upgrading performance evaluation

The membrane bundle composed of 33 zeolite membranes was tested for single gas permeation of He, H_2, CO_2, N_2, CH_4, and SF_6 at 0.3 MPa. The CO_2 permeance was significantly higher than that of the other gases and decreased with increasing kinetic diameter of the gas molecules (Fig. S27). The CH_4 permeance remained constant even when the pressure was increased to 1.1 MPa. Meanwhile, the bulky SF_6 molecules (kinetic diameter: ~0.55 nm) primarily permeate through the defective pores, exhibiting a low permeance of 1.2×10^{-10} mol·m^{-2}·s^{-1}·Pa^{-1} (0.36 GPU). Both results confirm that zeolitic pores dominate the gas transport pathway[44]. This leads to a superior high selectivity of 16 for CO_2/N_2, 170 for CO_2/CH_4, and 1380 for CO_2/SF_6, which is comparable to those of a single HF membrane[41]. This consistency proves the membrane bundle has minimal defects, maintaining the superior separation performance even after scaling up.

The separation performance was evaluated via stepwise pressurization of a binary CO_2/CH_4 mixture up to 4.0 MPa. Both CO_2 permeance and CO_2/CH_4 selectivity decreased with increasing pressure (Fig. 5a), which is a typical phenomenon of the adsorption-diffusion mechanism for zeolite membranes[45]. Importantly, the membrane exhibits fully reversible performance when depressurization back to ambient pressure, confirming the mechanical robustness. A comparison of different feeding directions shows that feeding from the substrate side (*tail*) results in lower CO_2 permeance and CO_2/CH_4 selectivity (Fig. S28a and Fig. 5b). This is attributed to severe concentration polarization in the support pores, which hinders efficient mass transfer to the selective membrane layer. Thus, feeding to the selective membrane layer side (head) is more favorable for the practical natural gas upgrading processes[46].

To further validate practical applicability, a pilot-scale biogas upgrading test was conducted using ten zeolite membrane bundles (Fig. 5c). Biogas containing 43% CO_2 from the fermentation tank was pressurized to 2.0 MPa and fed to the selective membrane side (head). For dry biogas feed, the average CO_2 permeance stabilized at ~4×10^{-8} mol·m^{-2}·s^{-1}·Pa^{-1} (~120 GPU) (Fig. 5d), which is only half of the value observed for a single bundle in laboratory tests. This is attributed to a high stage-cut of 40%, over 80% CO_2 permeated through the membranes, resulting in strong competitive CH_4 adsorption[47]. The IAST calculation further revealed that up to 55% of the transport pathways in zeolite membranes near the retentate outlet were occupied by CH_4 molecules (Fig. S29), directly inhibiting CO_2 adsorption and diffusion[48]. When the biogas was saturated with water vapor (partial pressure: 5.7 kPa, relative humidity = 100%), the CO_2 permeance further decreased to ~2×10^{-8} mol·m^{-2}·s^{-1}·Pa^{-1} (~60 GPU), indicating an extra drying procedure is required to keep the maximum permeance. The membrane simultaneously achieved water vapor removal with a permeance of 2.3×10^{-9} mol·m^{-2}·s^{-1}·Pa^{-1} (6.87 GPU), as evidenced by the reduced water partial pressure (1.9 kPa, relative humidity = 33%) in the retentate. The membrane maintained stable performance over a long-term test of >220 days, demonstrating superior resistance to water vapor, a high partial pressure of CO_2 and H_2S. The H_2S concentration in the retentate decreased from 2500 ppm to 300 ppm (Fig. 5e). These results validate the triple functions of zeolite membranes, which have high potential to eliminate the complicated pretreatment process (e.g., dehydration, desulfurization) required for commercial polymeric membranes[49]. Furthermore, the CO_2/CH_4 selectivity remained stable at ~22 throughout 43

https://doi.org/10.1038/s41467-026-70549-2

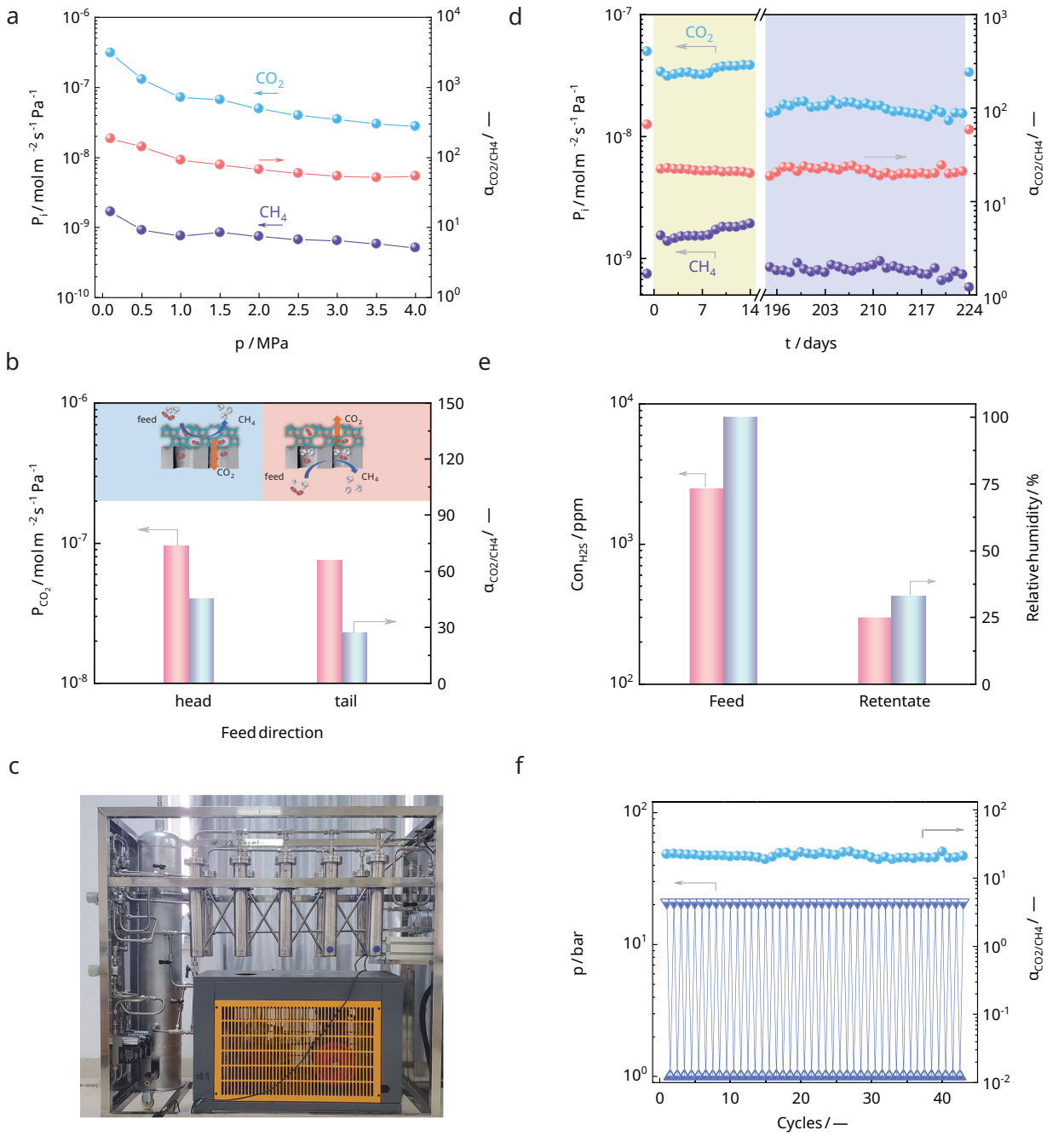

Fig. 5 | Biogas upgrading performance of large-area SSZ-13 zeolite membrane bundles. a High-pressure CO_2/CH_4 separation performance at a feed flowrate of 6 L·min^{-1}. **b** CO_2 permeance and CO_2/CH_4 mixture selectivity at 2.0 MPa feed to the zeolite membrane side (head, blue area) and to the porous support side (tail, red area). **c** Photo of a biogas upgrading system composed of ten zeolite membrane bundles. **d** Long-term stability for dry (yellow area) and humid (blue area) biogas upgrading. **e** Desulfurization of the biogas containing 2500 ppm H_2S. **f** Pressurization−depressurization cycle stability between 0.1 and 2.0 MPa. The biogas containing 43% CO_2: 55% CH_4 was provided by Xuzhou Huanneng Environmental Energy & Ecology Technology Co., Ltd., wherein the H_2S concentration ranged between 1000 ppm and 3000 ppm.

pressurization-depressurization cycles (Fig. 5f), confirming the mechanical robustness under industrially relevant biogas upgrading conditions.

In summary, we report an embryonic zeolite-mediated suture strategy for the thickness-controlled synthesis of highly selective zeolite membranes for tailored gas separation. This approach leverages the intrinsic reactive suturing capacity of embryonic zeolites to seamlessly integrate ball-milled seed particles into continuous and defect-minimized zeolite membranes. The membrane thickness is precisely controlled by the initial seed layer, eliminating the uncontrolled overgrowth that generally occurs in the conventional hydrothermal synthesis. This approach enabled the fabrication of thin (0.56 μm) SSZ-13 zeolite membranes that simultaneously achieve high CO_2 permeance (3000 GPU) and CO_2/CH_4 selectivity (158), which represents one of the state-of-the-art benchmarks for CO_2/CH_4 separation. Beyond lab-scale investigation, the EZMS strategy is applied to successfully synthesize zeolite membrane bundles composed of over 100 membranes (total area >0.5 m^2), all exhibiting

consistent separation performance and exceptional long-term stability (>220 days) under industrially relevant biogas upgrading. SSZ-13 zeolite membranes realized the simultaneous removal of CO_2, H_2S, and H_2O, eliminating the pretreatment steps mandatory for polymeric membranes. This reliable and scalable synthesis protocol, coupled with stable separation performance, contributes to the industrial deployment of zeolite membranes for gas separation.

Methods

Synthesis of SSZ-13 zeolite seeds

Typically, NaOH (Sinopharm Chemical Reagent Co., Ltd, AR) and $Al(OH)_3$ (Shanghai Lingfeng Chemical Reagent Co., Ltd., AR) were added into deionized water at room temperature and stirred for 2 h. Then a certain amount of TMAdaOH (25% in water) was added. Finally, colloidal silica was added dropwise into the solution. The final molar composition was 20 TMAdaOH: 16 NaOH: 0.5 Al_2O_3: 100 SiO_2: 4400 H_2O. The solution was transferred to a polytetrafluoroethylene (PTFE) lined autoclave and placed in an oven at 433 K for 96 h. After hydrothermal synthesis, the SSZ-13 crystals were recovered by centrifugation at 12840 g for 10 min and washed three times with deionized water. The powders were dried overnight at 333 K and calcined at 823 K for 24 h to remove the OSDA. The ball-milled seeds were prepared by ball-milling the pristine SSZ-13 zeolite with a planetary ball mill (Retsch Ind. Ltd., PM-100), using zirconium oxide balls as grinding media. The milling treatment was operated for 3 h at a rotating speed of 450 rpm.

Preparation of seed layers with different thicknesses

The four-channel α-Al_2O_3 hollow fibers were provided by Jiangsu Shining HiTech Co., Ltd., have outer/inner diameters (O.D./I.D.) of 3.8 mm/0.9 mm, porosity of ~40% and average pore size of 300 nm. Before seeding, they were ultrasonically cleaned for 2 h in deionized water and dried at 343 K overnight. The external surface was seeded with ball-milled SSZ-13 zeolite crystals by the dip-coating method. The top section of the hollow fibers was capped with Teflon tape, then they were vertically dipped into the seed suspensions as shown in Table S1 to prepare the seed layer with different thicknesses. The hollow fibers were dip-coated in an aqueous 0.5 wt% seed suspension for 15 s twice to get the seed layer with a thickness of ~2.5 µm. To reduce the seed layer thickness, a hollow fiber was vertically dipped into an aqueous 0.5 wt% seed suspension for 15 s to achieve a seed layer thickness of ~900 nm. Similarly, dipping the hollow fiber into the same suspension for 10 s resulted in a seed layer thickness of around 800 nm. When the hollow fiber was dipped into an aqueous 0.4 wt% seed suspension for 10 s, the seed layer thickness was about 700 nm. Finally, dipping the hollow fiber into an aqueous 0.3 wt% seed suspension for 15 s produced a seed layer with a thickness of ~560 nm. The seeded hollow fibers were dried at 343 K overnight before the membrane synthesis.

For the hollow fiber bundles, 17, 33, and 102 pieces of hollow fiber supports were assembled into a bundle unit with a dead-end flow configuration. One end of the unit is sealed with glaze, and the other end is open for gas flow. The effective length of the hollow fiber support is 40 cm.

Synthesis of SSZ-13 zeolite membranes

The precursor for membrane synthesis was prepared following the same procedure as the pristine SSZ-13 zeolite crystals. The molar composition was 20 TMAdaOH: 16 NaOH: 0.5 Al_2O_3: 105 SiO_2: 4400 H_2O. The precursor was aged at room temperature or 368 K in an oven for different periods. Then, the seeded hollow fibers or hollow fiber bundles, as mentioned above, were transferred to the precursor. The hydrothermal synthesis was conducted at 453 K for a certain period. After the crystallization at 453 K, the membranes were washed with DI water and dried overnight at 373 K. The template was removed by calcination in an ozone/oxygen atmosphere at 473 K for 72 h with a heating and cooling rate of 0.5 K·min^{-1}. Ozone was supplied by an electrical discharge generator (Lvbang, NPO50P−S−2). The ozone/oxygen gas mixture was fed at a flowrate of 4 L min^{-1}.

Synthesis of STT zeolite membranes

The STT-type zeolite membrane was prepared from a synthesis solution with a molar composition of 1 SiO_2: 0.2 TMAdaOH: 44 H_2O. The precursor was aged at room temperature or at 368 K in an oven for 72 h. The hydrothermal synthesis was conducted at 453 K for 24 h.

Synthesis of MFI zeolite membranes

The precursor solution for MFI-type zeolite membrane synthesis was prepared with a molar composition of SiO_2: TPAOH: H_2O = 1: 0.24: 178. Deionized water and tetrapropylammonium hydroxide (TPAOH) were first added to a PTFE bottle and stirred until homogeneous. Tetraethyl orthosilicate (TEOS) was then slowly added dropwise under continuous stirring. The precursor was aged at room temperature or 368 K in an oven for 48 h. The hydrothermal synthesis was conducted at 433 K for 14 h.

Gas separation test

The single gas permeation was tested using a transient permeation apparatus without sweep gas. The feed pressure was modulated by a back-pressure regulator, and the permeate side was operated under atmospheric pressure. A gas chromatography (GC, 8860 Agilent Technologies), equipped with a thermal conductivity detector (TCD) and a ShinCarbon column, was used to analyze gas compositions. The permeance of component i (P_i), ideal selectivity ($S_{i/j}$), and mixture selectivity ($\alpha_{i/j}$) of component i over component j is defined by the following equation:

$$P_i = \frac{J_i}{\Delta p_i} \tag{1}$$

$$S = \frac{P_i}{P_j} \tag{2}$$

$$\alpha_{ij} = \frac{y_i/y_j}{x_i/x_j} \tag{3}$$

Where J_i is the permeation flux through the membrane, mol·m^{-2}·s^{-1}; x_i (x_j) and y_i (y_j) are the molar fraction of component i (j) in feed and permeate, respectively. Δp_i is the trans-membrane partial pressure difference for component i (Pa). Considering the variation of gas composition along the membrane, we used the logarithmic average to calculate $(\Delta p_i)_{ln}$ (Pa)[45]:

$$(\Delta p_i)_{ln} = \frac{(p_i^{feed} - p_i^{perm}) - (p_i^{ret} - p_i^{perm})}{\ln\left(\frac{p_i^{feed} - p_i^{perm}}{p_i^{ret} - p_i^{perm}}\right)} \tag{4}$$

The methane loss is defined as:

$$CH_4\,\text{loss} = \frac{CH_4\,\text{flow in permeate}}{CH_4\,\text{flow in feed}} \tag{5}$$

The ratio of the total permeate over the total feed flowrate is defined as stage-cut:

$$\text{stage} - \text{cut} = \frac{\text{permeate flow}}{\text{feed flow}} \tag{6}$$

The relative humidity (RH) is defined as:

$$RH = \frac{\text{Actual vapor pressure}}{\text{Saturation vapor pressure}} \quad (7)$$

Characterization

The morphologies of zeolite seeds and membranes were observed by Field Emission Scanning Electron Microscopy (FE-SEM, S-4800, Hitachi). Before characterization, the samples were sputtered with platinum. The phase compositions were determined by powder X-ray diffraction (PXRD, MiniFlex 600, Rigaku) with Cu K_α radiation ($\lambda = 0.154$ nm at 40 kV and 15 mA) in the 2θ range of 5–50° with the scan speed of 10° min^{-1}. For the membrane sample, the membranes were cut into small segments and tightly pasted on the sample rack for PXRD characterization. 10 mg zeolite crystals were dispersed in 10 mL deionized water and then ultrasounded for 30 min to make it evenly dispersed for particle size distribution analysis by dynamic light scattering (DLS) method using Malvern ZS90. Fourier transform infrared (FTIR) spectra were recorded on a Nicolet™ Summit™ FTIR Spectrometer with a DTGS KBr detector. ATR-FTIR spectra were recorded on a Bruker alpha ii Compact FTIR spectrometer with Quick Snap™ Platinum-ATR Convenience sampling module. Solid-state MAS NMR experiments were conducted on a Bruker Avance Neo 400 Solid-State NMR Spectrometer.

Data availability

Data generated in this study are provided in the manuscript, or supplementary information and Source data are provided with this paper.

References

1. Park, H. B., Kamcev, J., Robeson, L. M., Elimelech, M. & Freeman, B. D. Maximizing the right stuff: the trade-off between membrane permeability and selectivity. *Science* **356**, eaab0530 (2017).
2. Carreon, M. A., Li, S., Falconer, J. L. & Noble, R. D. Alumina-supported SAPO-34 membranes for CO_2/CH_4 separation. *J. Am. Chem. Soc.* **130**, 5412–5413 (2008).
3. Ozcan, A. et al. Tuning MOF/polymer interfacial pore geometry in mixed matrix membrane for upgrading CO_2 separation performance. *Sci. Adv.* **10**, eadk5846 (2024).
4. Fan, W. et al. Multivariate polycrystalline metal–organic framework membranes for CO_2/CH_4 separation. *J. Am. Chem. Soc.* **143**, 17716–17723 (2021).
5. Liu, X., Wang, J., Shang, Y., Yavuz, C. T. & Khashab, N. M. Ionic covalent organic framework-based membranes for selective and highly permeable molecular sieving. *J. Am. Chem. Soc.* **146**, 2313–2318 (2024).
6. Maghsoudi, H. & Soltanieh, M. Simultaneous separation of H_2S and CO_2 from CH_4 by a high silica CHA-type zeolite membrane. *J. Membr. Sci.* **470**, 159–165 (2014).
7. Han, J. et al. Tuning the phase composition of metal-organic framework membranes for helium separation through incorporation of fullerenes. *J. Am. Chem. Soc.* **145**, 14793–14801 (2023).
8. Krishna, R. & Baur, R. Analytic solution of the Maxwell–Stefan equations for multicomponent permeation across a zeolite membrane. *Chem. Eng. J.* **97**, 37–45 (2004).
9. Zhou, S. et al. Asymmetric pore windows in MOF membranes for natural gas valorization. *Nature* **606**, 706–712 (2022).
10. Peng, Y. et al. Metal-organic framework nanosheets as building blocks for molecular sieving membranes. *Science* **346**, 1356–1359 (2014).
11. Wu, W. et al. Accurate stacking engineering of MOF nanosheets as membranes for precise H2 sieving. *Nat. Commun.* **15**, 10730 (2024).
12. Kim, D. et al. Twin-free, directly synthesized MFI nanosheets with improved thickness uniformity and their use in membrane fabrication. *Sci. Adv.* **8**, eabm8162 (2022).
13. Dakhchoune, M. et al. Gas-sieving zeolitic membranes fabricated by condensation of precursor nanosheets. *Nat. Mater.* **20**, 362–369 (2021).
14. Yang, S., Min, B., Fu, Q., Jones, C. W. & Nair, S. High-performance zeolitic hollow-fiber membranes by a viscosity-confined dry gel conversion process for gas separation. *Angew. Chem. Int. Ed.* **61**, e202204265 (2022).
15. Tang, X. et al. Efficient synthesis of thin SSZ-13 membranes by gel-less method. *J. Membr. Sci.* **620**, 118920 (2021).
16. Tang, X. et al. Fast synthesis of thin SSZ-13 membranes by a hot-dipping method. *J. Membr. Sci.* **629**, 119297 (2021).
17. Jiang, J. et al. Gel-modulated growth of high-quality zeolite membranes. *ACS Appl. Mater. Interfaces* **12**, 26095–26100 (2020).
18. Peng, X. et al. Improved synthesis of hollow fiber SSZ-13 zeolite membranes for high-pressure CO_2/CH_4 separation. *Angew. Chem. Int. Ed.* **63**, e202405969 (2024).
19. Yang, S., Chiang, Y. & Nair, S. Scalable one-step gel conversion route to high-performance CHA zeolite hollow fiber membranes and modules for CO_2 separation. *Energy Technol.* **7**, 1900494 (2019).
20. Wang, B. et al. Separation of light gas mixtures using zeolite SSZ-13 membranes. *Microporous Mesoporous Mater.* **275**, 191–199 (2019).
21. Li, Y. M. et al. High-performance 7-channel monolith supported SSZ-13 membranes for high-pressure CO_2/CH_4 separations. *J. Membr. Sci.* **629**, 119277 (2021).
22. Zhou, J. J., Wu, S. J., Liu, B., Zhou, R. F. & Xing, W. H. Scalable fabrication of highly selective SSZ-13 membranes on 19-channel monolithic supports for efficient CO_2 capture. *Sep. Purif. Technol.* **293**, 121122 (2022).
23. Huang, W. et al. Large surface-to-volume-ratio and ultrahigh selectivity SSZ-13 membranes on 61-channel monoliths for efficient separation of CO_2/CH_4 mixture. *Sep. Purif. Technol.* **311**, 123285 (2023).
24. Lee, P. S. et al. A zeolite membrane module composed of SAPO-34 hollow fibers for use in fluorinated gas enrichment. *J. Membr. Sci.* **542**, 123–132 (2017).
25. Jehannin, M., Rao, A. & Cölfen, H. New horizons of nonclassical crystallization. *J. Am. Chem. Soc.* **141**, 10120–10136 (2019).
26. Li, S. G. et al. Scale-up of SAPO-34 membranes for CO_2/CH_4 separation. *J. Membr. Sci.* **352**, 7–13 (2010).
27. Li, Y. et al. Highly efficient synthesis of high-silica SSZ-13 zeolite by interzeolite transformation of L zeolite at higher temperature. *J. Solid State Chem.* **293**, 121769 (2021).
28. Yu, L., Nobandegani, M. S. & Hedlund, J. Industrially relevant CHA membranes for CO_2/CH_4 separation. *J. Membr. Sci.* **641**, 119888 (2022).
29. Qiu, H. E. et al. High performance SSZ-13 membranes prepared at low temperature. *J. Membr. Sci.* **603**, 118023 (2020).
30. Chen, C.-T. et al. Reaction kinetics regulated formation of short-range order in an amorphous matrix during zeolite crystallization. *J. Am. Chem. Soc.* **143**, 10986–10997 (2021).
31. Wang, X. et al. Influence of an N,N,N-trimethyl-1-adamantyl ammonium ($TMAda^+$) structure directing agent on Al distributions and pair features in chabazite zeolite. *Chem. Mater.* **34**, 10811–10822 (2022).
32. Lim, I. H., Schrader, W. & Schüth, F. The formation of zeolites from solution–analysis by mass spectrometry. *Microporous Mesoporous Mater.* **166**, 20–36 (2013).
33. Joichi, Y. et al. Stepwise gel preparation for high-quality CHA zeolite synthesis: a common tool for synthesis diversification. *Cryst. Growth Des.* **18**, 5652–5662 (2018).

34. Kadja, G. T. M., Kadir, I. R., Fajar, A. T. N., Suendo, V. & Mukti, R. R. Revisiting the seed-assisted synthesis of zeolites without organic structure-directing agents: insights from the CHA case. *RSC Adv.* **10**, 5304–5315 (2020).
35. Wardani, M. K. et al. Highly crystalline mesoporous SSZ-13 zeolite obtained via controlled post-synthetic treatment. *RSC Adv.* **9**, 77–86 (2019).
36. Minami, A. et al. Tracking sub-nano-scale structural evolution in zeolite synthesis by in situ high-energy X-ray total scattering measurement with pair distribution function analysis. *J. Am. Chem. Soc.* **144**, 23313–23320 (2022).
37. Zhang, J. et al. Importance of controllable Al sites in CHA framework by crystallization pathways for NH_3-SCR reaction. *Appl. Catal. B* **277**, 119193 (2020).
38. Wang, L. et al. Embryonic zeolite-assisted synthesis of SSZ-13 with superior efficiency and their excellent catalytic performance. *J. Mater. Chem. A* **9**, 15238–15245 (2021).
39. Umeda, T. et al. Comparative study on the different interaction pathways between amorphous aluminosilicate species and organic structure-directing agents yielding different zeolite phases. *J. Phys. Chem. C* **121**, 24324–24334 (2017).
40. Bello, E. et al. NH_3-SCR catalysts for heavy-duty diesel vehicles: preparation of CHA-type zeolites with low-cost templates. *Appl. Catal., B* **303**, 120928 (2022).
41. Liu, H. et al. SSZ-13 zeolite membranes on four-channel α-Al_2O_3 hollow fibers for CO_2 separation. *Sep. Purif. Technol.* **267**, 118611 (2021).
42. Zhang, Q. et al. Silanol-engineered nonclassical growth of zeolite nanosheets from oriented attachment of amorphous protozeolite nanoparticles. *J. Am. Chem. Soc.* **145**, 21231–21241 (2023).
43. Zhang, Z. et al. Pilot-scale fabrication, separation performance and field test of tubular SSZ-13 membranes for efficient CO_2 separation. *Chem. Eng. Sci.* **284**, 119452 (2024).
44. Yu, L. & Hedlund, J. Large and highly selective and permeable CHA zeolite membranes. *Ind. Eng. Chem. Res.* **62**, 16058–16069 (2023).
45. Kosinov, N. et al. High flux high-silica SSZ-13 membrane for CO_2 separation. *J. Mater. Chem. A* **2**, 13083–13092 (2014).
46. van de Graaf, J. M., van der Bijl, E., Stol, A., Kapteijn, F. & Moulijn, J. A. Effect of operating conditions and membrane quality on the separation performance of composite Silicalite-1 membranes. *Ind. Eng. Chem. Res.* **37**, 4071–4083 (1998).
47. Li, Y., Yi, H., Tang, X., Li, F. & Yuan, Q. Adsorption separation of CO_2/CH_4 gas mixture on the commercial zeolites at atmospheric pressure. *Chem. Eng. J.* **229**, 50–56 (2013).
48. Krishna, R., Li, S., van Baten, J. M., Falconer, J. L. & Noble, R. D. Investigation of slowing-down and speeding-up effects in binary mixture permeation across SAPO-34 and MFI membranes. *Sep. Purif. Technol.* **60**, 230–236 (2008).
49. Chen, X. Y., Vinh-Thang, H., Ramirez, A. A., Rodrigue, D. & Kaliaguine, S. Membrane gas separation technologies for biogas upgrading. *RSC Adv.* **5**, 24399–24448 (2015).

Acknowledgements

This work is sponsored by the National Key Research and Development Program of China (2024YFB4006703, X.W.), the National Natural Science Foundation of China (22035002, 22378187, and U24A20533, X.G. and X.W.), Jiangsu Outstanding Youth Fund project (BK20240030, X.W.), Jiangsu 333 High Level Talent Training Project (X.G. and X.W.), Zhejiang Provincial Natural Science Foundation of China (2024SJCZX0021, X.G.), Quzhou Municipal Science and Technology Research Project (2024Z002, X.W.). We thank Prof. Wei Fan from the University of Massachusetts Amherst for the kind discussion.

Author contributions

X.W., X.G., F.K., and L.Y. conceived the idea and designed the experiments, analyzed the data, and wrote the manuscript. Y.J. and Y.F. synthesized and characterized the materials. Z.Z. performed the long-term stability test. X.P. performed the adsorption calculations. All the authors contributed to the scientific discussions and to the preparation of the manuscript.

Competing interests

The authors declare no competing interests.

Additional information

Supplementary information The online version contains supplementary material available at https://doi.org/10.1038/s41467-026-70549-2.

Correspondence and requests for materials should be addressed to Xuerui Wang or Xuehong Gu.

Peer review information *Nature Communications* thanks the anonymous reviewers for their contribution to the peer review of this work. A peer review file is available.